Optimized flow distributor for stabilized thermal stratification in a single-medium thermocline storage tank: A numerical and experimental study

Wanruo Lou, Arnaud Arrivé, Baoshan Xie, Julien Aubril, Yilin Fan, Lingai Luo

Optimized flow distributor for stabilized thermal stratification in a single-medium thermocline storage tank: A numerical and experimental study

Wanruo LOU[1], Baoshan XIE[1], Julien AUBRIL[1], Yilin FAN[1], Lingai LUO[1,*] Arnaud ARRIVE[1]

[1]Nantes Université, CNRS, Laboratoire de thermique et énergie de Nantes, LTeN, UMR 6607, F-44000 Nantes, France

Abstract

This paper investigates the impact of flow injection on the temperature stratification inside single-medium thermocline storage tanks. Special focus is given on how to maintain the stable thermocline evolution during the dynamic charging or discharging operation, by using a new type of fluid diffuser, namely the Ring-Opening Plate Distributors (ROPDs). Firstly, the ROPDs are designed and the size distribution of the ring-shape openings is optimized by a simulation-based optimization algorithm. This diffuser concept has then been validated experimentally, showing its effectiveness in improving the charging and discharging efficiency of a laboratory-scale storage tank by up to 14.5% and 19.8%, respectively.

Systematic experiments are performed to examine the effects of the injecting flow rate and temperature on the local transient temperature profiles and on the energy and exergy efficiencies of the thermocline tank. The stability range of operational parameters, characterized by the bulk Froude number ($Fr<3$), has been determined for quasi-undisturbed advance of the thermocline. Beyond this stability range, simple tube-type diffuser is no longer capable of mitigating the impact of inflowing thermal jet. Additional structuration and optimization of the diffuser geometry become essential to stabilized the thermal stratification and to maintain a good thermal performance of the storage tank.

Keywords: Single-medium thermocline (SMT); Thermal energy storage (TES); Ring-Opening Plate distributor (ROPD); Flow distribution; Thermal stratification; optimization.

* Corresponding author
Email address: lingai.luo@univ-nantes.fr (L. Luo)

Nomenclature

Latin letters

Cp	Heat capacity at constant pressure [J·kg^{-1}·K^{-1}]
D	Diameter of tank [m]
d	Diameter of inlet/outlet port [m]
E	Energy [J]
Ex	Exergy [J]
e	Thickness of the baffles [m]
Fr	Froude number [-]
g	Gravitational acceleration [m s^{-2}]
H	Height of thermocline tank [m]
P	Pressure [Pa]
$\dot{m}$	Mass flow rate [kg·s^{-1}]
Q	Flow rate [L·min^{-1}]
r	Opening center location [m]
Re	Reynolds number [-]
s	Opening surface area [m^2]
T	Temperature [K]
T^*	Dimensionless temperature [K]
t	Time [s]
t^*	Dimensionless time [–]
$\bar{t}$	Mean value of all passage times [K]
v	Velocity [m·s^{-1}]
$\bar{v}$	Mean velocity [m·s^{-1}]
V	Volume [m^3]
V^*	Dimensionless volume [-]
w	Width of the ring-shape opening [m]

Greek symbols

η	Efficiency [–]
λ	Thermal conductivity [W·m^{-1}·K^{-1}]
μ	Viscosity [kg m^{-1} s^{-1}]
ρ	Density [kg m^{-3}]
ΔT	Temperature difference [K]

Subscripts/superscripts

bottom	Bottom
c	Cold temperature
ch	Charging
h	Hot temperature
in	Inlet
manifold	Manifold
max	Maximum
normal	Normal
out	Outlet
residence	Residence time
stored	Stored
tank	Thermocline tank
thermocline	Thermocline zone
x, y	Coordinates
0	Reference

Abbreviations

CFD	Computational Fluid Dynamics
HTF	Heat transfer fluid
i.d.	Interior diameter
ROPD	Ring-Opening Plate Distributor
SMT	Single-medium thermocline
TC	Thermocouple
TES	Thermal energy storage

1. Introduction

The energy transforming in conformity with sustainability goals requests the prompt uptake of renewables within a majority of energy demand domains [1,2]. Thermal energy storage (TES) has the considerable potential to realize high shares of renewable energy in different sectors, such as power generation, industries and buildings [3,4]. Beneficial features of TES including variable storage capacity and duration, flexible decoupling of supply/demand, adaptable integration manners [5] and life cycle advantages have attracted special attentions from various energy markets. According to the IRENA's Paris Agreement-aligned transforming energy scenario [6], it is expected that the installed TES capacity would be increased threefold in the next 10 years, from 234 GWh in 2019 to at least 800 GWh in 2030.

Current available TES systems can be classified into two-tank or single-tank concept [7], differentiate themselves by involving two individual tanks or only one tank for storing and circulating the heat transfer fluids (HTFs). For the latter, hot and cold HTFs are separated naturally by the density difference, with the presence of a temperature transition zone between them called the *thermocline*. A techno-economic assessment [8] showed that the single-tank thermocline technology could result in levelized cost of storage about 48% lower than that of two-tank concept, thereby receiving increased attention worldwide.

The operation of a thermocline-based storage tank is generally composed of three stages: the charging (energy storage), the stand-by and the discharging (energy release). As for the charging, the hot HTF is introduced into the top port of the storage tank, driving the cold HTF out from the bottom port. The opposite fluid direction is proceeded for the discharging operation. The interval time period between the charging and the discharging is called the stand-by. A thermal stratification zone with temperature gradient, the thermocline, exists between hot and cold HTFs. Besides the heat loss from the storage tank to the ambient [9], the overall performance of the thermocline storage tank depends largely on the level of thermal stratification [10]. To achieve a highly-efficient charging/discharging operation, the thermocline decay (de-stratification) should be reduced to the least possible extent with a small volume occupied by this temperature transition zone [11].

Nevertheless, the heat transfer always takes place at interface of the hot and cold HTFs which are in direct contact. Especially during the dynamic charging or discharging process, the inflowing HTF jet with different velocity and temperature (density) will disturb the pre-staying calm fluid inside the tank. Besides the diffusion heat transfer due to the temperature gradient, the heat convection caused by this sudden injection and the subsequent mixing motion could also be a dominant factor that degrades the temperature stratification [12]. The impact of this injecting flow could be more prominent for single-medium thermocline (SMT) storage tanks than dual-medium ones [13]. Without the buffering effect of solid fillers, the fluid mixing region could occupy a large volume of the SMT tank, sometimes even the whole tank under high flow rate condition [14]. Given the fact that SMT storage tanks are commonly employed for the space heating and cooling of both individual buildings and

districts/communities due to their volume compactness, simple construction and easy maintenance [15], researches have been devoted to study the impacts of flow injection on the stability of thermocline evolution and to propose measures to mitigate the performance degradation.

To overcome the limitations of simple inlet/outlet ports in handling the sudden flow injection in SMT storage tanks, great efforts have been made on the use of structured flow diffusers as alternative. The general strategy is, with the help of specially structured flow distributors, to produce multi-branch streams (e.g., [16,17]), inversed flow (e.g., [18–20]) or radial flow (e.g., [21–23]), so as to alleviate the disturbances brought by the strong momentum-dominated inflowing jet. The Froude number Fr (cf. Eq. 17), together with the Reynold number Re (cf. Eq. 15) are usually used to indicate the hydrodynamic conditions of the inlet design. Chung et al. [24] numerically tested different types of diffusers (radial plate, adjusted plate and H-beam) and showed the negligible influence of Fr whereas governing influence of Re and diffuser on the thermal performance of the storage tank. Karim [25] experimentally tested octagonal-shape diffusers with different opening areas and showed that the design should be based on Fr=1 while lower Fr could cause unequal flow from different openings. García-Marí et al. [26] reported better thermal performance of a hot water storage tank by using a sintered bronze microspheres diffuser compared to a conventional inlet elbow, regardless of the flow rate tested. Wang and Davidson [27] experimentally tested the performance of a rigid porous-tube stratification manifold and showed that the jet mixing could be basically eliminated in comparison with an inlet pipe. Hosseinnia et al. [28] numerically showed that a cluster of parallel-disks diffusers could guarantee a low momentum induced mixing and a small thermocline thickness. In contrast, Bahnfleth and Song [29] showed that the double-ring slotted pipe diffuser, despite designed and tested within the recommended Fr and Re limits, could still result in significant thermocline degradation due to large scale convection. The experimental study of Li et al. [16] showed the worse performance of structured distributor (shower-type) than simple slotting-type and direct inlets, under their testing conditions. Chandra and Matuska [30] systematically compared a slotted diffuser, a perforated diffuser and a simple inlet device and found that the slotted diffuser represented outstanding performance only at high flow rate. In short, the performance improvement of the proposed flow distributor designs seems much more meaningful according to the practical operating conditions.

Many studies have thereby focused on the effect of process parameters (e.g., flow rate, temperature difference) on overall performance of the SMT storage tank, with the purpose of determining the suitable operating conditions [31]. The numerical study of Dehghan and Barzegar [14] clearly illustrated the impact of discharging flow rate on the flow mixing. The mixing region was confined at the bottom region of the tank at low flow rate (Re_{in}=100) but expanded directly towards the top outlet port at high flow rate (Re_{in}=1000). Yaïci et al. [32] tested different flow rates (0.05-0.2 kg·s^{-1}) and reported that the thermocline deterioration might be more pronounced at low flow rates whereas the flow mixing could be intense when the flow rate increased to a certain value. An optimal flow rate could exist due to the competition between the effect of mixing and thermal diffusion [32]. By using a novel boxed flow equalizer, Wang et al. [33] showed that the thermal stratification improved

first and then reduced with the increasing injecting flow rate. Lou et al. [34] also reported that the heat diffusion could be responsible for thermocline degradation at low flow rate due to the lengthened operation time. As for the effect of temperature difference between the injected fluid and the pre-existing fluid (ΔT) in the SMT tank, researchers' opinions are less unanimous. Nelson et al. [35] reported the reduced mixing region and the enhanced thermal stratification at a larger ΔT. This is mainly due to the stronger buoyancy force at the higher density difference that could better compensate the inertial force of the injecting HTF. Nevertheless, the heat exchange due to diffusion turns to be more important at larger ΔT, especially under long charging/discharging time. In this sense, the study of Yaïci et al. [32] showed negligible impact of ΔT on the formation and evolution of the thermocline during the charging. Shaikh et al. [36] showed the enlarged thermocline thickness at a larger ΔT, despite the reduced penetration distance of the entering jet. Moreover, Advaith et al. [15] revealed that the influence of ΔT could also be related to the ambient temperature of the storage tank due to the inevitable heat loss.

The above literature survey indicates that the design and implementation of flow distributors deserve particular attention to achieve stabilized thermal stratification in SMT storage tanks. However, most of the studies still stay on the numerical or experimental testing of a certain type of flow diffuser by varying one or several geometric parameters. Studies involving the simulation, the structure optimization and the experimental verification of flow distributors under a wide range of working conditions are still rare. Moreover, the separate influence of the operating parameters (e.g., inlet flow rate; ΔT) as well as their combined effects on the thermal stratification and thermocline evolution need further clarification, as controversy still exists in the published literature. Therefore, systematic investigations with experimental feedback are of great interest to understand impact of thermal jet and to determine the stability range for certain inlet structures.

As a continuation and extension of our previous study [34], this work has firstly presented the structure optimization of a new type of flow diffuser, namely the Ring-Opening Plate Distributors (ROPDs), to mitigate the thermocline degradation caused by the thermal jet in SMT storage tanks. We strive to bridge the computational fluid dynamics (CFD)-based optimization procedure for both upper and bottom ROPDs and the experimental testing results of a lab-scale prototype for both the charging and discharging operations. Then, a systematic experimental investigation into the performances of the storage tank equipped with or without ROPDs has been performed. The influences of the inlet flow rate and the temperature difference on the local transient temperature profiles and on the energy and exergy efficiencies have been compared and analyzed. The stability range of operational parameters, characterized by the bulk Fr number, has been determined for maintaining quasi-undisturbed advance of the thermocline. Beyond this stability range, the optimized ROPDs have shown to be capable of maintaining high charging/discharging efficiency of the storage tank. The findings of this work can help provide design guidelines on flow diffusers and determine adapted operational conditions for practical applications of SMT storage tanks with optimized performance.

2. Experimental set-up

2.1. SMT storage tank and Ring-Opening Plate Distributor (ROPD)

The SMT prototype is a vertical cylindrical storage tank having an inner diameter (D) of 194 mm and inner height (H) of 390 mm, the H/D ratio thus being 2.0. The upper or bottom port (i.d.: 10 mm) is situated in the center of the upper or bottom cover, respectively (Fig. 1), rendering it an axisymmetric geometry that could be simplified into 2D in the CFD-based optimization. The tank body was made of polycarbonate (ABAQUEPLAST), having a good temperature resistance (up to 125 °C) and a low thermal conductivity (0.2 $W \cdot m^{-1} \cdot K^{-1}$). The thickness of the lateral wall is 3 mm while that for upper and bottom covers is 12 mm.

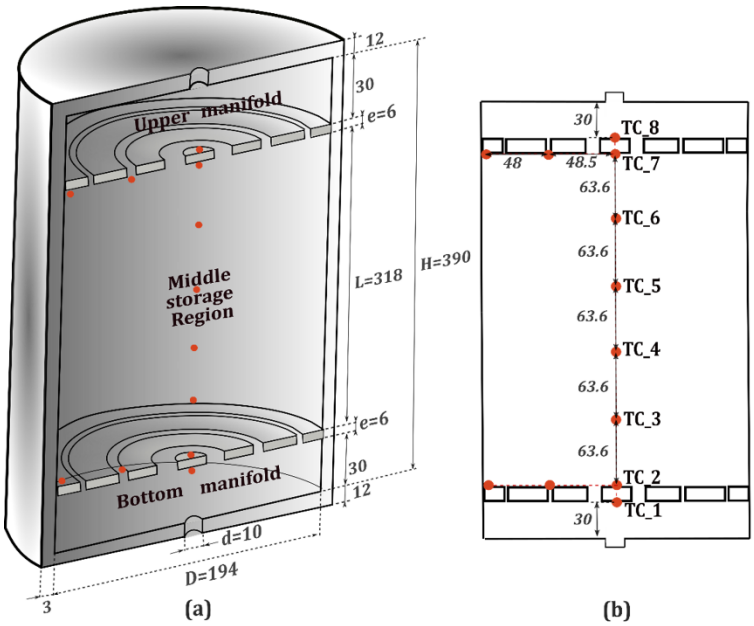

Figure 1. Geometry and dimensions of the cylindrical SMT storage tank for laboratory testing (unit: mm). (a) schematic view; (b) vertical cross-section and arrangement of the thermocouples

Two plates with ring-shape openings also made of polycarbonate were installed into the tank, dividing the inner tank body into three parts as shown in Fig. 1(a): the upper manifold (30 mm in height), the middle zone (318 mm in height) and the bottom manifold (30 mm in height). The disc-like ring-opening plates have an overall dimension of 194 mm in diameter and 6 mm in thickness. Each plate has three ring-shape openings, their widths subjected to optimization as will be described later. The translucent silica gel (Loctite 5366) was used to seal up the border between the plates and the tank wall so that the fluid can pass from one zone to another only through the ring openings.

Twelve thermocouples TC (RS PRO type K 1/0.3mm; ±0.35 K) were used to measure the fluid temperature at different positions, as shown in Fig. 1(b). Among them, TC_1/TC_8 right facing the upper/bottom ports were mainly used to monitor the inflowing fluid temperature before touching the upper/bottom plate during the charging or discharging operation, respectively. TC_2-7 also located on

the central axis were installed to record the axial fluid temperature variation, evenly spaced 63.6 mm between one another. All the TCs were attached to a slender I-shape plastic support, which was fixed at the upper and the bottom plates.

2.2. Test-rig and experimental procedure

The test-rig shown in Fig. 2 is composed of the thermocline tank, hot and cold circuits, a feed tank and the control & data acquisition system. The HTF used in this study was water. Each water tank (THERMOR Steatis-100L) was equipped with a closed loop driven by a fluid circulator (GRUNDFOS ALPHA120-50N150) to ensure the inside homogenous water temperature. A built-in heater strip (1200 W maximum) was installed inside the hot water tank as the heat source while a cryo-thermostat (LAUDA Proline-RP845) connected to a home-made helical-coil heat exchanger inside the cold water tank was used as the cold source. Temperature sensors PT100 (RS 762-1134; ±0.35 K) were installed inside both water tanks to measure the water temperature. The output fluid from each water tank was firstly filtered by a 20 μm filter (HNP Mikrosysteme F-MI2-T), and then delivered by a gear pump (TUTHILL Pump P-series, 0.067-7.63 $L \cdot min^{-1}$) to the thermocline tank (or feed tank). The flow rate of each circuit was measured by a flowmeter (Kobold DPM 1150-G2, 0.05-5 $L \cdot min^{-1}$; ±1%) installed downstream of the pump. The feed tank (300L) was used to store and recycle the HTFs. Two additional PT100 sensors (RS 891-9145; ±0.35 K) were imbedded into the upper and bottom ports of the thermocline tank to measure and monitor the inlet/outlet temperature of the HTF.

Both the charging and discharging operations were investigated. Each operation was composed of several steps, briefly described as follows (charging as example).

(1) Preparation: the water quantity was ensured to be sufficient inside both water tanks. The closed loops for water heating and cooling were then turned on.

(2) Filling-up: once the temperature set points in water tanks were reached, the gear pump 2 was started to deliver the cold water into the thermocline tank from the bottom to the top until the tank was full of the cold water at T_c.

(3) Preheating: the gear pump 1 was started to deliver the hot water to preheat the piping between the hot water tank and the thermocline tank. The purge water was guided to the feed tank via the 3-way electric valve (ASCO SCG327B001) at the top (inlet) port of the thermocline tank. The purpose of this step was to eliminate the possible temperature and flow-rate fluctuations of the inflowing hot water during the short start-up period due to the existing (cold) water in the connection pipe.

(4) Once the constant flow rate (Q_{in}) and preset temperature (T_h) had been reached, the 3-way valve at the top (inlet) port was switched on to inject the hot water into the thermocline tank. The charging operation continued till the tank was fully occupied by the hot water.

The discharging process followed basically the same protocol, except that the bottom port was switched to be the inlet whereas the upper port became the outlet.

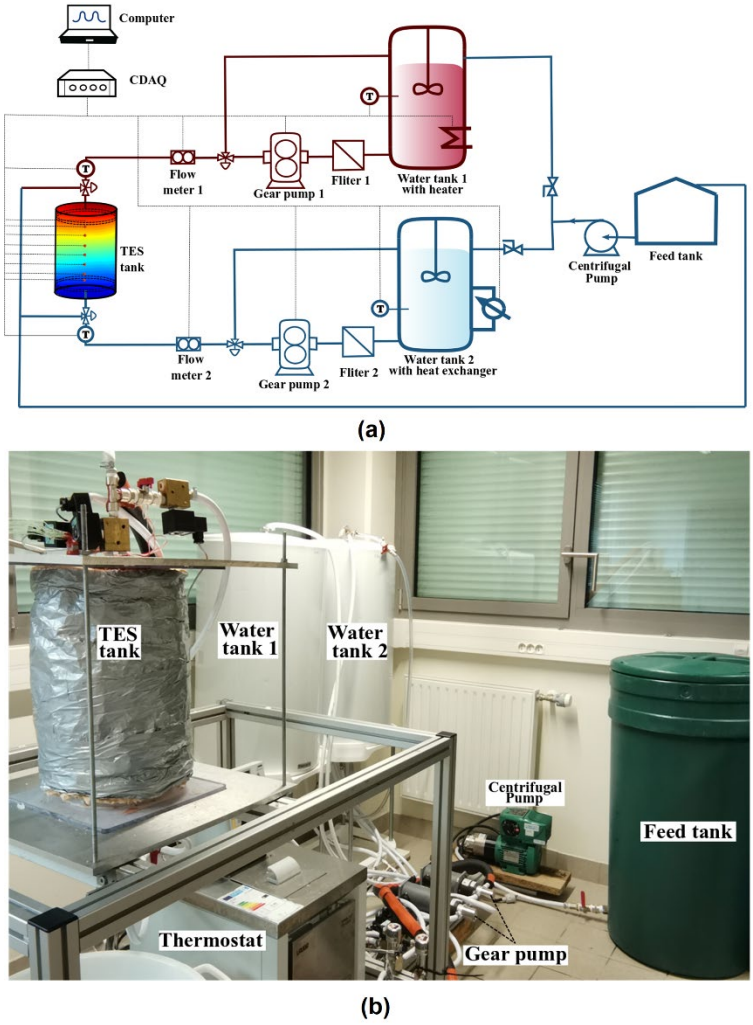

Figure 2. Test-rig for the cylindrical SMT storage tank. (a) schematic diagram; (b) photo view

The tested charging/discharging flow rate (Q_{in}) ranged between 0.3 and 1.5 L·min^{-1}, corresponding to Re_{in} from 946 to 4812 and an average tank Reynolds number (Re_{tank} defined in Eq. 16) from 50 to 251. The tested hot temperature T_h ranged from 323.15 K to 343.15 K while the cold water temperature T_c was kept at 293.15 K, the ΔT being 30-50 K. Note that charging and discharging were performed separately, without addressing the cyclic operation issue.

The tank body as well as the pipes and valves for entering the hot fluid were well-insulated by foamglass to reduce the heat loss at a minimum level. The tightness of the setup was verified before every test to avoid the water leakage. A LabVIEW program developed in-house, together with the data acquisition system (NI cDAQ 9178) and the modules was used to control and regulate the output of two gear pumps (NI9265), the heater strip (NI9265), the cryo-thermostat and all electric valves (NI9474), and to record the real-time measurement data of PT100 (NI 9217), TCs (NI 9213) and flowmeters (NI 9209) during the whole charging or discharging process.

2.3. CFD Model and validation

2.3.1. Simulation parameters

CFD simulations were performed to calculate the transient fluid velocity & temperature characteristics in the tank which were then used for the configuration optimization of the ROPDs. 2D-axisymetric fluid domain (Fig. 3) adapted to the cylindrical tank geometry was employed. The thermophysical properties of water are considered as temperature dependent and the fitting correlations used in the simulations are listed in Table 1.

Table.1. Thermo-physical properties of water (293.15 K<T<343.15 K) [37,38]

Property	Unit	Fitting correlation T (K)
Density ρ	kg·m^{-3}	$739.57 + 1.9908T - 0.0038\,T^2$
Specific heat C_p	J·kg^{-1}·K^{-1}	$5438.6 - 8.07T + 0.0129T^2$
Thermal conductivity λ	W·m^{-1}·K^{-1}	$-0.7888 + 0.0077T - 1 \times 10^{-5}\,T^2$
Viscosity μ	Pa·s^{-1}	$0.0215 - 1.198 \times 10^{-4}\,T + 1.701 \times 10^{-7}\,T^2$

ANSYS FLUENT 19.1 was used for the CFD simulations. The operational pressure was fixed at 101325 Pa. The gravity effect was considered while the viscous heating effect was neglected. k-ε RNG turbulent model considering the buoyancy effect was used to simulate the flow behaviors and thermal stratification [18,39]. The SIMPLE algorithm was applied for the pressure-velocity coupling. The standard spatial discretization scheme was used for pressure due to relatively small pressure gradient in the flow. The second-order upwind scheme was used for the discretization of momentum, energy, k and ε equations.

The initial conditions and the boundary conditions were set as follows (charging as example).

(i) The initial conditions were zero velocities and uniform temperature.

$$v_x = 0;\ v_y = 0; T = T_c \tag{1}$$

(ii) At inlet, hot HTF (T_h) was injected into the upper port at t_0 moment of charging.

$$v_y|_{y=in} = -v_{in} \tag{2}$$

$$T_y|_{y=in} = T_h \tag{3}$$

Fully developed velocity profile was used for v_{in} to better reflect the real testing condition (piping and inlet tube upstream the numerical inlet boundary):

$$v_{in} = v_{in_{max}}\left[1 - \frac{(x^2)}{\left(\frac{d}{2}\right)^2}\right], x \in [0, \frac{d}{2}] \tag{4}$$

Where d is the diameter of the inlet and $v_{in_{max}}$ is twice of the mean inlet velocity.

(iii) Zero gauge pressure outlet at the (bottom) outlet port:

$$P_{out} = 0 \tag{5}$$

(iv) Axis boundary for y-axis (x=0):

$$v_{normal} = 0 \tag{6}$$

(v) Other walls were all set as adiabatic, including top, bottom and lateral walls of TES tank as well as upper and bottom plates. For example, at the lateral wall:

$$\frac{\partial T}{\partial x}\Big|_{x=\frac{D}{2}} = 0 \tag{7}$$

The boundary settings for the discharging was almost the same, except that the positions of inlet and outlet were interchanged. The initial condition for the fluid domain was zero velocities and uniform temperature at T_h.

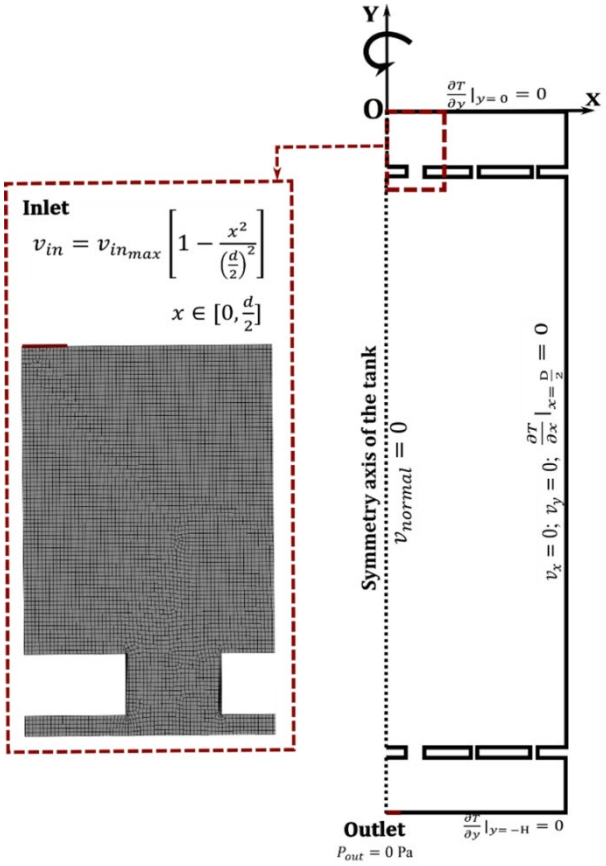

Figure 3. 2D axisymmetric fluid domain, the mesh and the boundary conditions (charging for example).

Simulations were performed under transient state with fixed time step of 0.001 s considering both the computational cost and the calculation accuracy. The solution was considered to be converged when (i) normalized residuals were smaller than 10^{-5} for mass, momentum, k and ε equations and 10^{-7} for energy equation, and (ii) the inlet gauge pressure become constant (less than 0.5% variation).

2.3.2. Mesh model, grid independency and experimental validationThe structured quad mesh was used, with inflation layers and additional local refinement for parts with large flux gradient. A grid independence study was performed with the total number of elements increasing from 0.2 million to 0.38 million. The comparison on the calculated mean passage time $\bar{t}$ (Eq. S1) and on the inlet gauge

pressure was shown to be inferior to 0.01% when the number of elements was higher than 0.2 million. After considering both the calculation time and precision, the mesh used in this study had approximately 0.23 to 0.25 million elements relying on different ROPD configurations. Simulations were then carried out by a workstation with 2.2 GHz Intel processors (Xeon CPU E5-2630 v4) and 32 GB RAM. A calculation time up to 72 hours was required for each simulation of fully charging or discharging in order to better capture the tailing effect of different distributor geometries. Compared to full 3D simulation of the SMT storage tank, the calculation time has been significantly reduced due to the use of axisymmetric 2D model.

The numerical model was validated by comparing with our experimental results of the thermocline tank (conditions: T_h=333.15 K, T_c=293.15 K, Q_{in} = 1 L·min^{-1}, initial ROPDs, charging). The temperature profiles at 8 positions of the central axis measured by TC_1-8 were compared with the simulated data, as shown in Fig. 4. In general, good agreement on the global tendency of the thermocline movement between the simulation and experimental results could be observed.

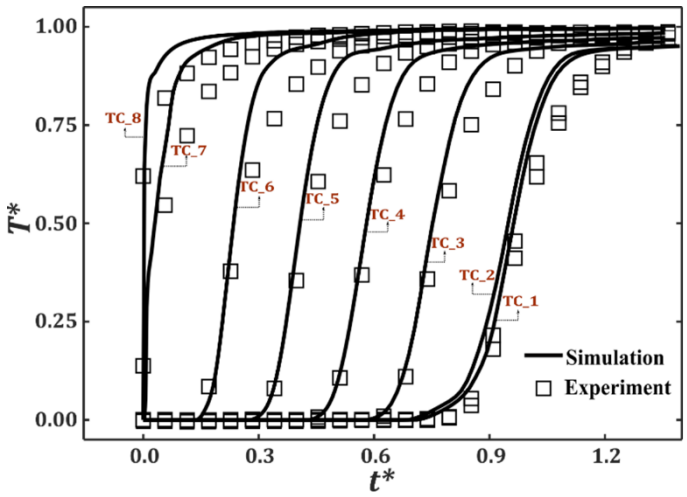

Figure 4. Comparison of the CFD and experimental results on the temperature profiles inside the thermocline tank. Conditions: T_h=333.15 K, T_c=293.15 K, Q_{in} = 1 L·min^{-1}, initial upper & bottom ROPDs, charging

2.4. Parameter definition and uncertainty analysis

The theoretical charging/discharging time of the storage tank ($t_{residence}$) is defined as the fluid residence time (plug flow) of the storage tank, calculated by the ratio of the total tank volume (V_{tank}=11.2 L) and the volume flow rate (Q_{in}):

$$t_{residence} = \frac{V_{tank}}{Q_{in}} \tag{8}$$

Similarly, the theoretical charging/discharging time of the upper/bottom manifold ($t_{manifold}$) could be calculated by:

$$t_{manifold} = \frac{V_{manifold}}{Q_{in}} \tag{9}$$

Where $V_{manifold}$ is the volume of the upper/bottom manifold (0.89 L). The charging/discharging time and the temperature are normalized as follows:

$$t^* = \frac{t}{t_{residence}} \tag{10}$$

$$T^* = \frac{T - T_0}{T_h - T_c} \tag{11}$$

Where T_0 is the reference temperature [40] (293.15 K for this study).

The dimensionless thermocline volume $V^*_{thermocline}$ is defined as the volume proportion of the storage tank occupied by the thermocline (Eq. 12). Here the threshold values [T_{20}; T_{80}] were used to identify the temperature borders or fronts of the thermocline zone [41] calculated by Eqs. (13) and (14).

$$V^*_{thermocline} = \frac{V_{[T20;T80]}}{V_{tank}} \tag{12}$$

$$T_{20} = T_c + 20\% \times (T_h - T_c) \tag{13}$$

$$T_{80} = T_c + 80\% \times (T_h - T_c) \tag{14}$$

The Reynolds number at the inlet port and at the tank body can be calculated by Eqs. 15 and 16, respectively.

$$Re_{in} = \frac{\rho \bar{v}_{in} d}{\mu} \tag{15}$$

$$Re_{tank} = \frac{\rho \bar{v}_{tank} D}{\mu} \tag{16}$$

Where D is the inner diameter of the tank. For simplification, the physical properties (ρ and μ) of water at 313.15 K were used for the calculation.

The bulk Froude number (Fr), defined as the ratio of the inertia force and the buoyancy force, is calculated by Eq. (17) [42].

$$Fr = \frac{\bar{v}_{in}}{\sqrt{dg(\rho_c - \rho_h)/\rho_c}} \tag{17}$$

Where ρ_c is the density of cold fluid at 293.15 K, ρ_h is the density of hot HTF ranging from 323.15 K to 343.15 K and g the gravitational acceleration.

Performance indicators based on both first and second law of thermodynamics are introduced to evaluate the performance of the SMT storage tank. The energy storage (or charging) efficiency (η_{ch}) presents the ratio of the effective storage energy to the overall inflowing energy to the storage tank [43].

$$\eta_{ch} = \frac{E_{in} - E_{out}}{E_{in}} = \frac{\int_0^t \dot{m} C_p (T_{in} - T_{out}) dt}{\int_0^t \dot{m} C_p (T_{in} - T_0) dt} \tag{18}$$

Where $\dot{m}$ is the mass flow rate and E is the transported energy through the inlet/outlet port.

The energy release (or discharging) efficiency (η_{dis}) indicates the ratio between the released energy from the storage tank and the overall stored energy.

$$\eta_{dis} = \frac{E_{out} - E_{in}}{E_{stored}} = \frac{\int_0^t \dot{m} C_p (T_{out} - T_{in}) dt}{E_{stored}} \tag{19}$$

For charging, the inlet exergy (Ex_{in}) and outlet exergy (Ex_{out}) are defined as [44]:

$$Ex_{in} = \int_0^t \dot{m}C_p\,[(T_{in} - T_0) - T_0\,(\ln\tfrac{T_{in}}{T_0})]\,dt \quad (20)$$

$$Ex_{out} = \int_0^t \dot{m}C_p\,[(T_{out} - T_0) - T_0\,(\ln\tfrac{T_{out}}{T_0})]\,dt \quad (21)$$

The transferred exergy during the charging/discharging is calculated by:

$$Ex_{ch} = Ex_{in} - Ex_{out} = \int_0^t \dot{m}C_p\,[(T_{in} - T_{out}) - T_0\,(\ln\tfrac{T_{in}}{T_{out}})]\,dt \quad (22)$$

$$Ex_{dis} = Ex_{out} - Ex_{in} = \int_0^t \dot{m}C_p\,[(T_{out} - T_{in}) - T_0\,(\ln\tfrac{T_{out}}{T_{in}})]\,dt \quad (23)$$

The maximum transferable exergy for the discharging process (Ex_{max}) is calculated by:

$$Ex_{max} = \int_0^t \dot{m}C_p\,[(T_{max} - T_0) - T_0\,(\ln\tfrac{T_{max}}{T_0})]\,dt \quad (24)$$

Where T_{max} is estimated as the mean value of all thermocouples inside the thermocline tank at t_0 of the discharging. The exergy efficiency η_{ex} is calculated by Eq. (25) [45].

$$\eta_{ex} = \frac{Ex_{dis}}{Ex_{max}} \quad (25)$$

Using the uncertainty propagation method for error analysis, the measuring uncertainty was estimated to be 1.45% for η_{ch}, 1.56% for η_{dis}, and 1.5% for η_{ex}, respectively.

3. ROPD: CFD-based optimization and experimental verification

3.1. Optimization of ROPD configuration

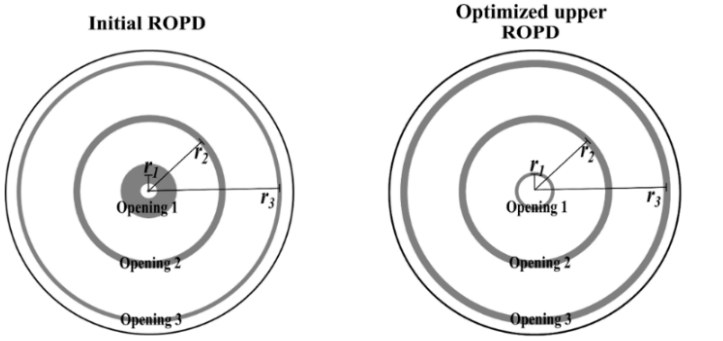

	Opening centerline location $[r_1, r_2, r_3]$ (mm)	Opening width $[w_1, w_2, w_3]$ (mm)	Opening surface $[s_1, s_2, s_3]$ (mm^2)
Initial ROPD	[16.2, 48.5, 80.8]	[10.378, 3.460, 2.076]	[1054, 1054, 1054]
Optimized upper ROPD		[2.512, 3.642, 3.566]	[254, 1105, 1803]
Optimized bottom ROPD		[2.362, 3.644, 3.570]	[240, 1110, 1812]

Figure 5. Geometry and dimensions of the initial and optimized ROPDs. Conditions: T_h=333.15 K, T_c=293.15 K, Q_{in} = 1 L min^{-1}

The structure optimization of the upper and bottom ROPDs is mainly based on the CFD-based algorithm proposed and developed in our earlier study [34]. The basic idea is to adjust the size of the ring openings on the disc-like plate so that the thermal front could pass through every opening simultaneously during a charging/discharging process. Detailed explanation of the optimization strategy and the numerical algorithm can be found in supplementary material (S1) of this paper. The initial and optimized geometry and dimensions of the ROPDs are presented in Fig. 5.

3.2. Numerical results

In order to provide a deeper insight into the fluid flow and heat transfer behaviors subjected to different inlet/outlet structures, the virtual streamslice superimposed over velocity contours and the fluid temperature cartographies at $t^*_{manifold}$ moment of charging (or discharging) process are displayed in Fig. 6. Five combinations of upper & bottom diffusers are simulated and compared, including simple inlet/outlet ports (S1 for charging), initial upper & bottom ROPDs (S2 for charging), optimized upper & initial bottom ROPDs (S3 for charging), optimized upper & initial bottom ROPDs (S4 for discharging) and optimized upper & bottom ROPDs (S5 for discharging).

Vortices are clearly visible on the velocity field of S1, due to the momentum-dominated flow injected from the upper port. The density difference between hot and cold fluids induces the buoyancy force that will interact with the inertia force, resulting in the rising of hot fluid in the form of plumes. The hot buoyant plumes will then mix with the surrounding cold fluid and be cooled down by convection. It can be observed from Fig. 6(S1) that the thermal jet could penetrate into a large depth of the tank (y=-120 mm) and the thermocline occupies a large volume (almost 30%) of the storage tank.

The installation of the initial upper ROPD could restrict, to some extent, the impact of the inflowing thermal jet within the upper manifold, where the vortices and the flow recirculation could be clearly seen (Fig. 6(S2)). Nevertheless, a small stream of the momentum-dominated hot flow 'leaks' from the upper manifold into the middle zone through the first opening close to the central axis of the tank. This "leakage" will cause the invasion of the thermal front to a certain depth of the middle zone (y=-72 mm) at $t^*_{manifold}$ while a large part of the upper manifold is still occupied by the cold fluid, as shown in the temperature cartography of Fig. 6(S2).

This disruptive flow leakage could be largely eliminated by optimizing the configuration of the upper ROPD, i.e., by narrowing the first ring opening near the central axis while widening the other two. The unexpected factors disturbing the temperature stratification (e.g., forced convection, buoyancy-driven eddy advection, instabilities of density/velocity, etc.) are by and large limited within the upper manifold. Therefore, the thermocline zone shows a thin and flattened shape, maintaining the stable thermal stratification, as displayed in Fig. 6(S3).

Shown in Fig. 6(S4) is actually the inverse (discharging) operation of the same combination for S3. But the fluid and temperature fields are similar to those of S2 because the bottom ROPD for

managing the cold inflowing jet has not been optimized. The 'leaking' stream still invades the middle zone but the (cold) thermal front penetrates with a smaller depth (y=-328 mm) compared to that for charging (S2). The gravity force could partly alleviate the strong inertia force of the entering jet.

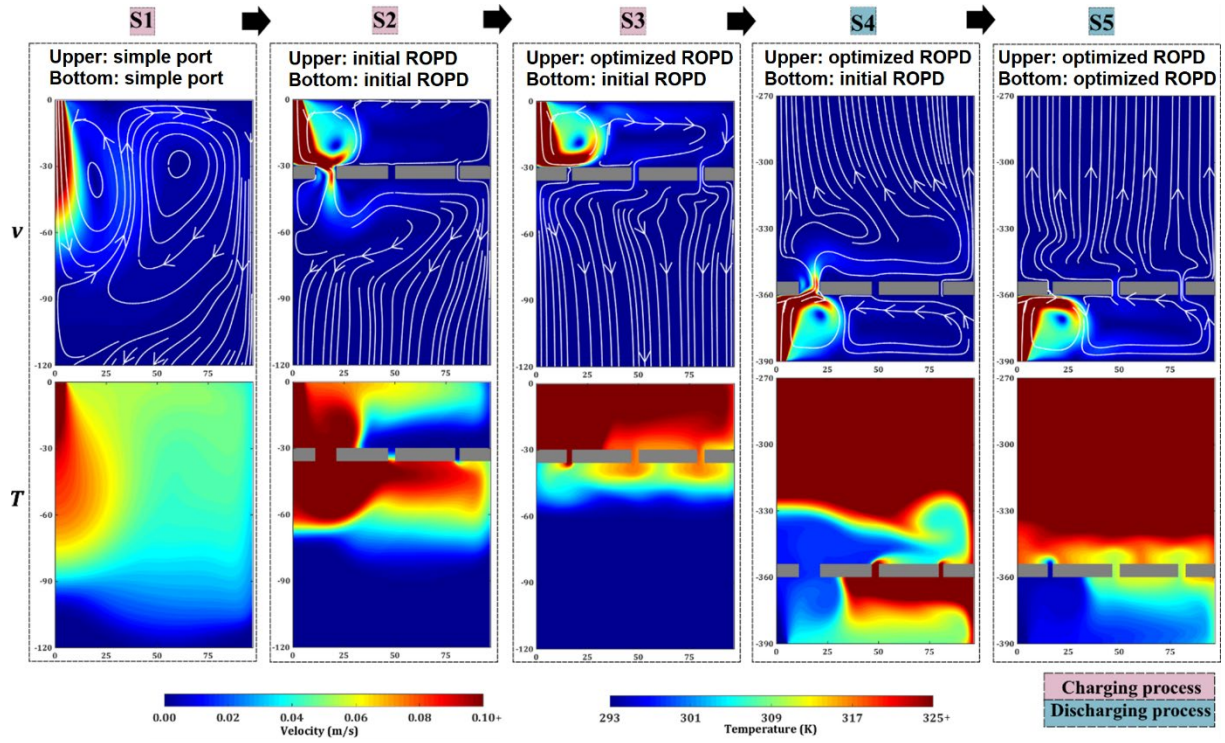

Figure 6. Velocity contour, streamslice and temperature cartography of the fluid domain at $t^*_{manifold}$ moment for different combinations of upper and bottom ROPDs. Conditions: T_h=333.15 K, T_c=293.15 K, Q_{in} = 1 L min^{-1}

Fig. 6(S5) displays the flow and temperature fields of the storage tank equipped with the optimized bottom ROPD for the discharging operation, analogous to the inverse of that shown in Fig. 6(S3). Again, the optimized ring-opening configuration could result in a regular and flat thermocline, successfully maintaining the temperature stratification at a high level.

In order to explore in depth the effect of ROPD configuration on the alleviation of the thermocline decay, the time-evolution of $V^*_{thermocline}$ for each combination of ROPDs is plotted in Fig. 7 and briefly commented as follows. Logically, the $V^*_{thermocline}$ for S1 case is the largest at almost all time. The increasing $V^*_{thermocline}$ curve for S4 is very similar to that for S2 but with a slight smaller value at the same t*. This is because of the positive contribution of the gravity effect as discussed above. The $V^*_{thermocline}$ curves for S3 and S5 increase first and then stabilize around the $t^*_{manifold}$, indicating that the thermocline expansion due to the inflowing thermal jet could be largely limited in the manifold. After $t^*_{manifold}$, the thermocline enclosed by the thermal fronts [T_{20}; T_{80}] traverses the optimized ring-opening plate and arrives calmly and stably into the middle zone.

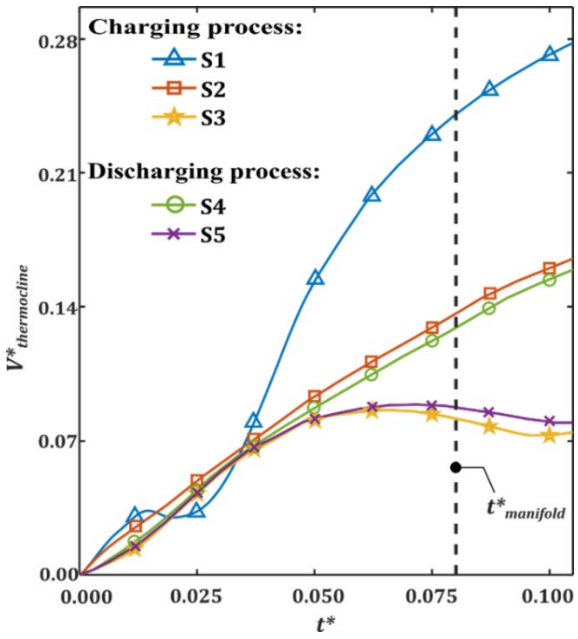

Figure 7. Evolution of the dimensionless thermocline volume $V^*_{thermocline}$ for different tested combinations of ROPDs. Conditions: T_h=333.15 K, T_c=293.15 K, Q_{in} = 1 L min^{-1}

3.3. Experimental verification

To verify the numerical results obtained, ROPDs were fabricated in-house and experiments were performed using the cylinder thermocline tank. Three combinations of ROPDs were tested and compared including S1 (without ROPDs), S2 (initial upper & bottom ROPDs) and S5 (optimized upper & bottom ROPDs), under the same condition for the optimization ($T_h = 333.15$ K, $T_c = 293.15$ K, $Q_{in} = 1$ L min^{-1}) for both charging and discharging operations. The temperature profiles measured by TC_2-6 at the axis of the middle zone during the charging process are plotted in Fig. 8, all showing the typical shape of S-curve as displayed by the top explicative image. Four periods of a thermocline charging operation could then be identified based on the climbing trend of the T^* curve, including (i) initial charging period [t_0 to $t^*(T^* = 0.2)$]; (ii) thermocline period [$t^*(T^* = 0.2)$ to $t^*(T^* = 0.8)$]; (iii) tailing period [$t^*(T^* = 0.8)$ to $t^*(T^* = 0.99)$] and (iv) fully charging period [$t^* > t^*(T^* = 0.99)$]. The temporal demarcation depends actually on the threshold temperatures of the thermocline and in this study it is [T_{20}; T_{80}].

The temperature profile of the perfectly stratified thermal plug-flow is also added in Fig. 8, providing a comparison between ideal and real-world operations. The early rise and the flat slope of the T^* curves at the thermocline period for S1, S2, S5 compared to the ideal profile indicate clearly the existence of the thermocline with a certain thickness due to the inevitable heat transfer between the hot and cold fluids. Note that the rising time $t^*(T^* = 0.2)$ implies the advance speed of (cold) thermal front whereas the duration of the thermocline period (or the slope of T^*) indicates the thickness of the thermocline at the central axis. In this regard, by comparing T^* curves of the three ROPD combinations, it can be inferred that the stratification levels are not identical. On the one hand, the T^* profile for S5

shows the latest rising moment, indicating that the calm cold environment in the middle zone could be held for the longest period before the arrival of the thermocline. On the other hand, its slope is also the steepest, implying the fastest passage of the thermocline with the highest temperature gradient.

The discharging operation has also been performed for these three combinations, and similar general trend could be observed (cf. Fig. S3 in supplementary material).

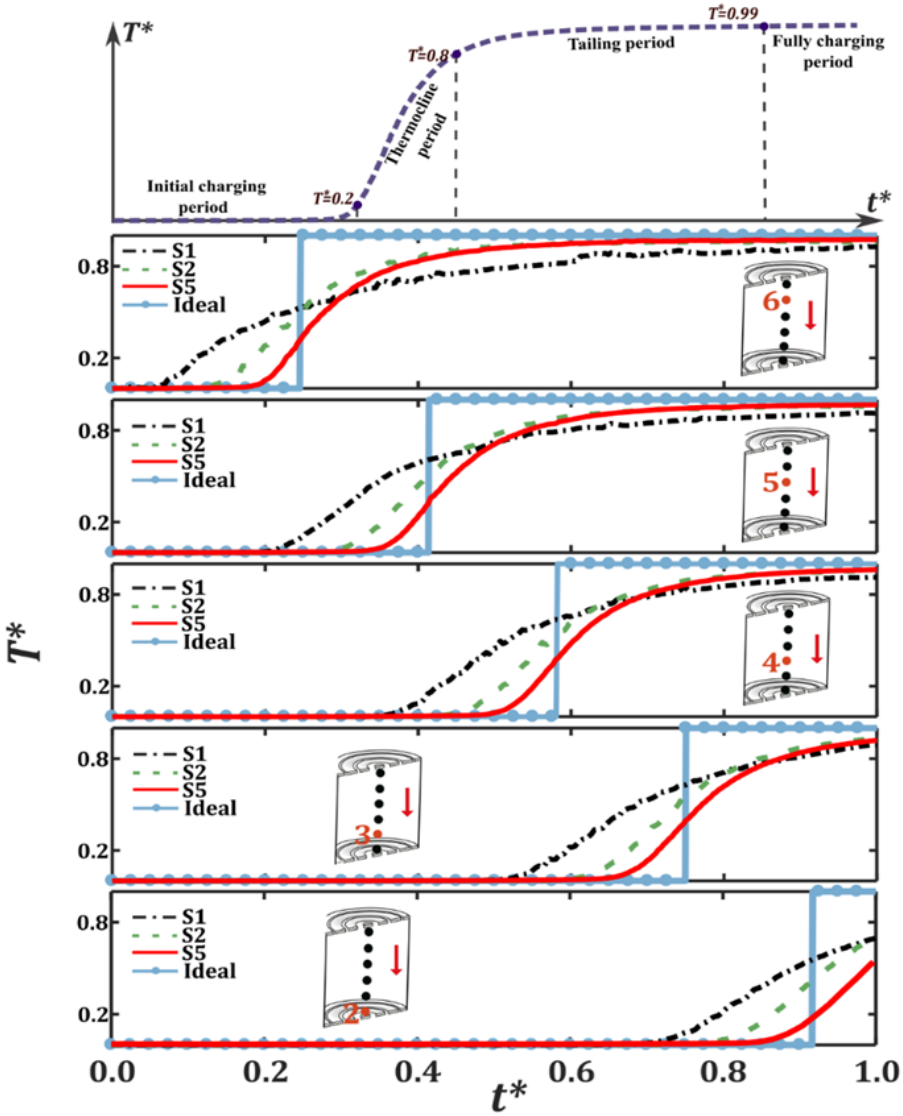

Figure 8. Dimensionless temperature T* versus dimensionless charging time t* for different tested combinations of ROPDs. Conditions: T_h=333.15 K, T_c=293.15 K, Q_{in} = 1 L min^{-1}

In Figs. 9(a) and 9(b) plotted the normalized outlet temperature T^*_{out}, also called the cut-off temperature, versus t^* and the charging efficiency η_{ch} versus T^*_{out}, respectively. Both the steeper slope of the T^*_{out} curve and the higher values of η_{ch} for S5 case indicate the improved thermal performance of the storage tank by equipping the optimized ROPDs. Fig. 9(c) shows the transferred exergy Ex_{ch} versus

T^*_{out}. It is worth noting that the Ex_{ch} rises very fast at the final stage of charging for S1, i.e., when $T^*_{out} > 0.8$. Apparently, the pronounced tailing phenomenon, i.e., very slow rise of the T^*_{out} greatly impacts the charging performance of the storage tank. On the one hand, the convective heat transfer due to fluid mixing will cause the irregular and distorted shape of the thermocline, making it much more difficult to timely drain out the cold fluid through the bottom port. On the other hand, the largely prolonged real charging time needed to reach the fully charged condition (tailing period as explained on top image of Fig. 8) results in the non-negligible heat loss to the ambient despite the insulation. Therefore, the fully charged condition of the SMT storage tank is neither easy nor cost-effective to achieve when the impact of the flow injection cannot be appropriately handled.

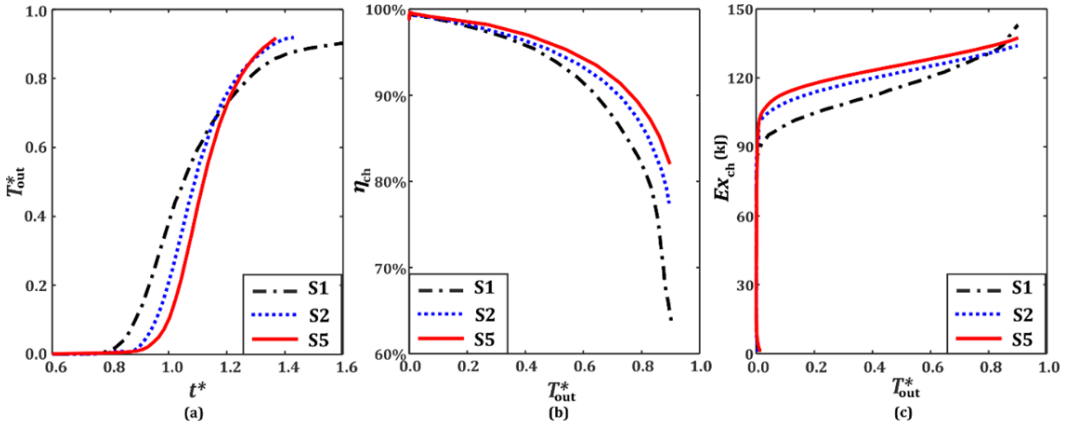

Figure 9. Comparison on the charging performance of the SMT storage tank with different combinations of ROPDs. (a) dimensionless outlet temperature T^*_{out} versus dimensionless charging time t*; (b) charging efficiency η_{ch} versus T^*_{out}; (c) transferred exergy Ex_{ch} versus T^*_{out}. Conditions: T_h=333.15 K, T_c=293.15 K, Q_{in} = 1 L min^{-1}

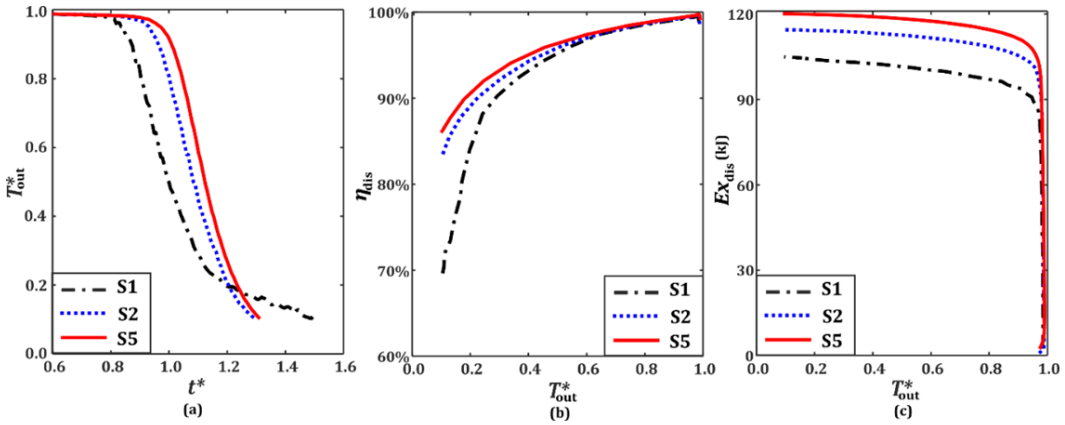

Figure 10. Comparison on the discharging performance of the SMT storage tank with different combinations of ROPDs. (a) dimensionless outlet temperature T^*_{out} versus dimensionless discharging time t*; (b) discharging efficiency η_{dis}versus T^*_{out}; (c) transferred exergy Ex_{dis} versus T^*_{out}. Conditions: T_c=293.15 K, T_h=333.15 K, Q_{in} = 1 L min^{-1}.

Figures 10(a) and 10(b) show T^*_{out} versus the dimensionless discharging time t^* and the discharging efficiency η_{dis} versus T^*_{out} for three tested combinations of ROPDs. Similar conclusion could be drawn, i.e., the largely improved η_{dis} by using the optimized ROPDs. The prominent mixing motion for S1 case causes significant convection heat transfer, thereby expanding the thermocline and lowing the η_{dis}. The transferred exergy Ex_{dis} versus T^*_{out} is plotted on Fig. 10(c), showing that for a given T^*_{out}, the Ex_{dis} for S5 is always the highest among the three tested combinations. No important rising of Ex_{dis} at the final stage of discharging despite the still existing tailing phenomena for the S1 case. This is because the T^*_{out} at the final stage of discharging is closer to the ambient temperature, the heat loss is thereby limited. In conclusion, both the numerical and experimental results show that the optimized ROPDs are really effective to improve the charging/discharging performance of the SMT storage tank.

4. Influences of operating parameters: a sensitivity study

Additional charging and discharging experiments were performed for the same thermocline storage tank and the three combinations of ROPDs (S1, S2 and S5) under different flowrate (Q_{in}=0.3, 0.5, 1.0 and 1.5 L·min^{-1}) and hot fluid temperature (T_h = 323.15, 333.15 and 343.15 K) conditions. The aim of this part of study is on one hand, to clarify the separate influence of the operating parameter as well as their combined effects on the temperature stratification, and on the other hand, to test the robustness of the optimized ROPDs subjected to varied operating conditions.

4.1. Local temperature evolutions

The T^* value measured by TC_6, TC_4 and TC_2 are plotted against t^* in Figs. 11 (for different T_h) and 12 (for different Q_{in}), monitoring the thermocline evolution in different positions of the tank during the charging operation.

By examining the Fig. 11, one may observe that all solid T^* curves (S5) have the steepest slope, the dashed curves (S2) come as the second, and the cross marker curves (S1) are the flattest. The stabilization of the thermal stratification by the ROPDs could be again highlighted. The impacts of the T_h (or ΔT) on the thermocline evolution are not the same when different ROPDs are installed. Higher ΔT leads to relatively later rise and steeper slope of the T^* curve for S1, due to the larger buoyancy force that contributes positively to balance out the inertial force of the inflowing jet. Meanwhile, the T^* curves of S5 case are almost overlapping, indicating that when optimized ROPDs are used, the temperature difference has little impact on the thermocline behaviors. The T^* curves for the discharging operation analogous to Fig. 11 is shown in Fig. S4 of the supplementary material and similar tendency and findings could be reached.

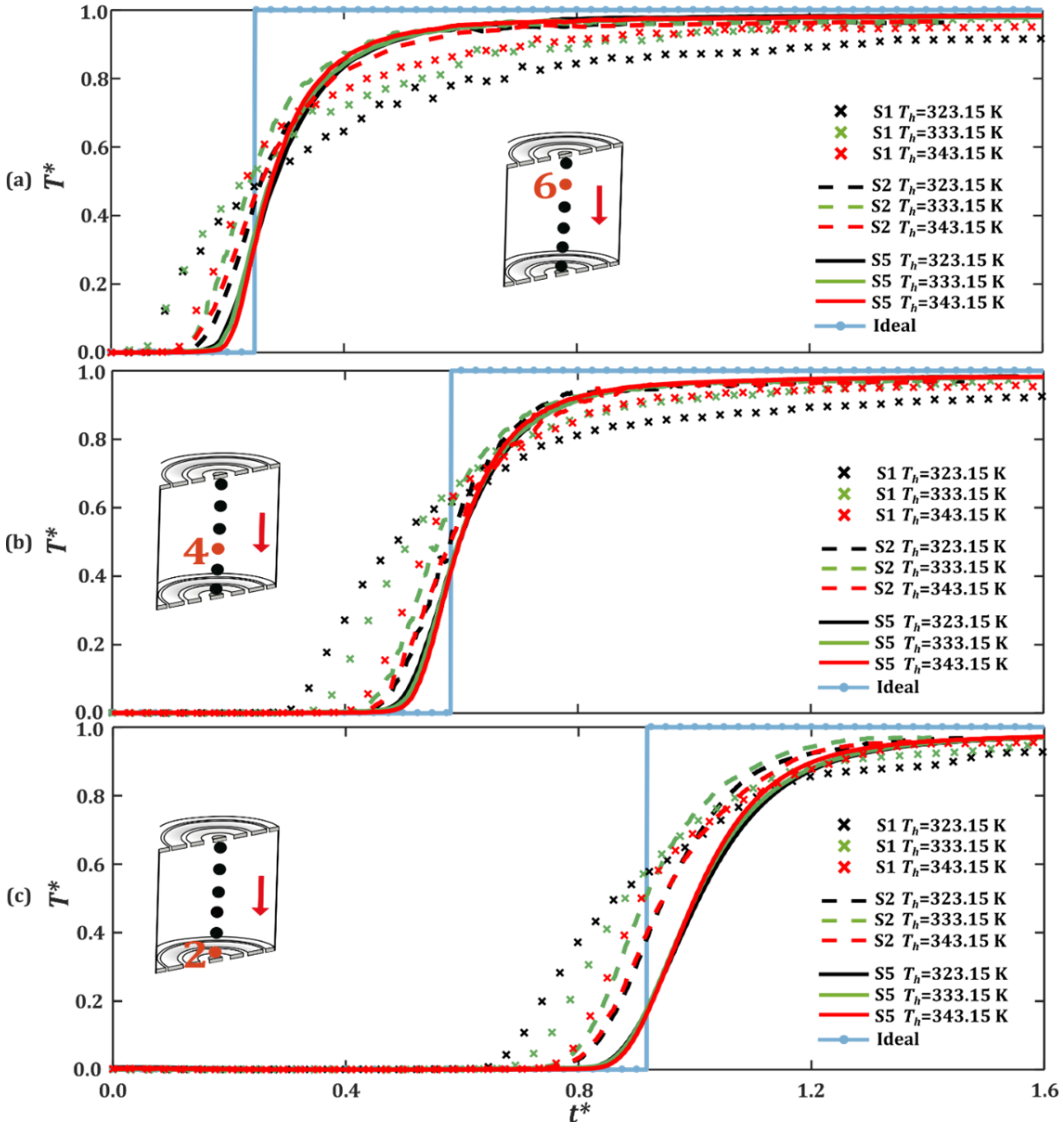

Figure 11. Effect of the inlet temperature T_h on the thermocline advance in the middle zone of the SMT tank equipped with different combinations of ROPDs. (a) T^* profile at TC_6; (b) T^* profile at TC_4; (c) T^* profile at TC_2. Conditions: T_c=293.15 K, Q_{in} = 1 L min^{-1}, charging.

The sensitivity/robustness of the optimized ROPDs over the operating flow rate (Q_{in}) is shown in Fig. 12. In general, the low Q_{in} renders a steeper slope of the T^* curve, indicating smaller impacts of inlet mixing and more regular and calmer thermocline evolution. For this condition, the benefit of ROPDs on the performance improvement is marginal, as will be quantified later when analyzing some global performance indicators. For higher flow rates (Q_{in}>1.0 L min^{-1}; Re_{tank}>167), simple inlet/outlet port (S1) is apparently incapable of handling the strong momentum-dominated inflowing jet, indicated by the early rising as well as the lengthened tailing period shown in Fig. 12.

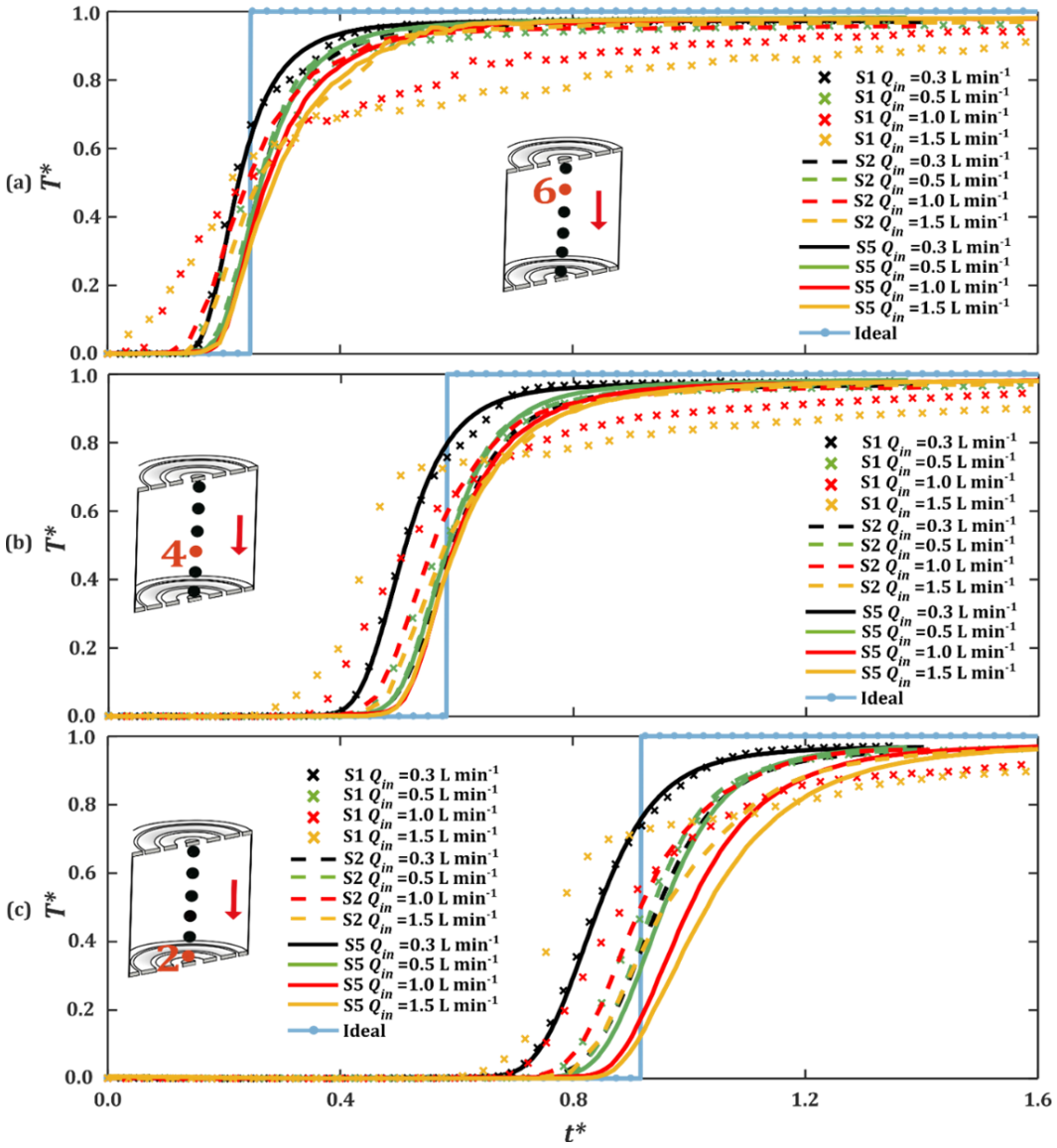

Figure 12. Effect of the flow rate Q_{in} on the thermocline advance inside the tank equipped with different combinations of ROPDs. (a) *T profile at TC_6; (b) *T** profile at TC_4; (c) *T** profile at TC_2. Conditions: T_h=333.15 K, T_c=293.15 K, charging**

For Q_{in}> 0.5 L min^{-1}, the T^* curves of S1 case rise always the earliest, followed by those of S2 case while those of S5 case rise the latest. This is in line with the simulation results as indicated by the temperature cartography in Fig. 6. Nevertheless for Q_{in}=0.3 L min^{-1}, later rise of S2 than S5 and S1 could be observed from Fig. 12. This is because of the small vertical penetration but more pronounced horizontal mixing due to the buoyancy-driven eddy advection. The opening size distribution of S2 facilitates this flow horizontal movement, resulting in the delayed rising time at the axis position.

For S1 case, the ranking of rising time is firstly 1.5<1.0<0.3<0.5 L·min^{-1} (TC_6) and later 1.5<0.3<1.0<0.5 L·min^{-1} (TC_2). This is due to the interaction of inertia force and the buoyancy force and their relative strengths throughout the movement of the thermocline. While for S5 case, the ranking

of rising time is 0.3<0.5<1.0<1.5 L·min^{-1}. With the optimized size of ring-openings (narrowed opening close to the center and widened one close to the lateral wall), the central vertical injecting flow is obstructed by the upper plate but directed horizontally to fully occupy the upper manifold. And the higher the Q_{in}, the stronger the inertia force and thereby the injecting flow is more likely to pass earlier through the lateral opening. The (cold) thermal front will presents a curved (parabolic) shape instead of the flat shape, resulting in the delayed advance of the thermal front at the central axis.

The T^* curves for the discharging analogous to Fig. 12 is shown in Fig. S5 of the supplementary material. Similar tendency but with small differences may be found, as being further commented there. More information and detailed discussions on the shape evolution of thermocline subjected to different opening configurations under certain *Re* condition may be found in [34].

4.2. Energy and exergy efficiencies

To further explore the global performance of the thermocline tank, energy and exergy efficiencies are analyzed and discussed. To facilitate the comparison, the thermal threshold is taken to be 20%, i.e., the cut-off $T^*_{out} = 0.80$ for the charging and $T^*_{out} = 0.20$ for the discharging, respectively.

Figure 13 shows the calculated charging or discharging efficiency of the storage tank base on different combinations of ROPDs and under various testing conditions. The bulk *Fr* numbers are also calculated and shown for analysis. Among the three tested combinations, S5 is always the one rendering the highest charging or discharging efficiency throughout all tested ranges of Q_{in} and ΔT. Compared to S2, η_{ch} could be improved by up to 3.6% where as η_{dis} could be improved by up to 2.9% by optimizing the size of the ring-openings. Compared to S1, the improvement is much more significant especially under high Q_{in}, reaching 14.5% for η_{ch} and 19.8% for η_{dis}, respectively. The use of initial ROPDs (S2) is beneficial compared to simple inlet/outlet ports (S1) at relatively high flow rate ($Q_{in} \geq 1$ L min^{-1}) but less performant than optimized ROPDs (S5). Under relatively low flow rate ($Q_{in} \leq 0.5$ L min^{-1}) however, the initial ROPDs might provide counterproductive work (additional flow disturbance caused by the ring-opening plates), indicated by lower values of η_{ch} compared to those of S1.

In Fig. 13, the separate effect of Q_{in} or ΔT on the global performance of the SMT storage tank can also be figured out. For the charging, the impact of ΔT is straightforward for all three combinations: a larger ΔT favors the thermal stratification to achieve a higher η_{ch}. For the discharging however, the influence of ΔT seems less significant, except for S1 case at relatively high flow rate ($Q_{in} \geq 1$ L min^{-1}) under which the difference can still be noticed. A great influence of Q_{in} could be found for S1, i.e., the charging or discharging efficiency falls sharply at $Q_{in} \geq 1$ L min^{-1}. Relatively marginal influence of Q_{in} may be observed for S2 and S5. The installation of ROPDs, especially after configuration optimization, could efficiently manage the flow and temperature disturbances brought by the strong momentum-dominated inflowing thermal jet.

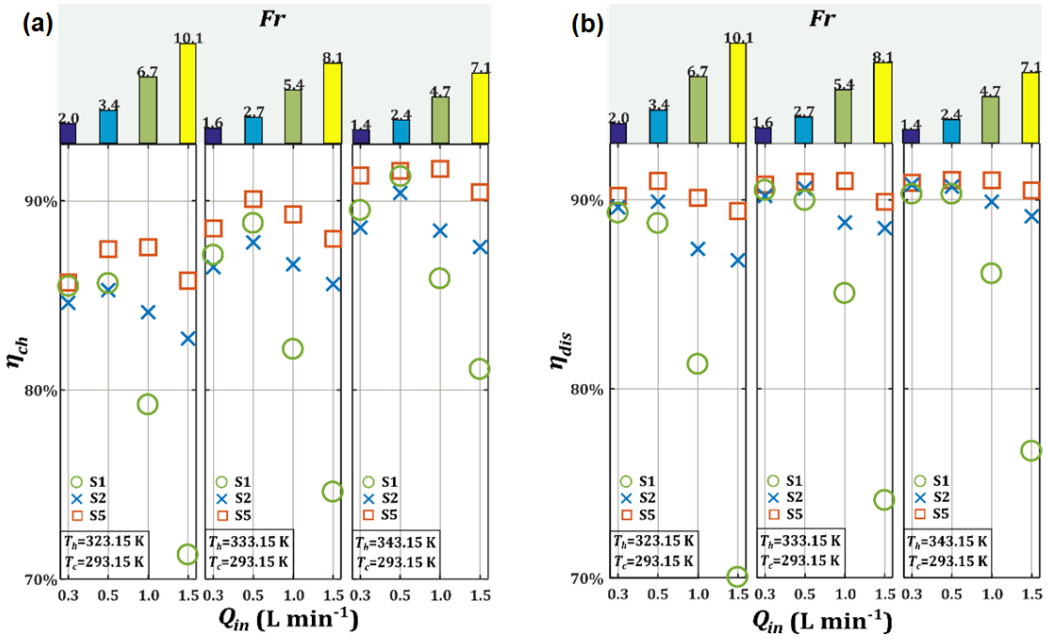

Figure 13. Charging efficiency (a) and discharging efficiency (b) of the SMT storage tank equipped with different combinations of ROPDs. Conditions: T_h=323.15, 333.15, and 343.15 K, T_c=293.15 K, Q_{in} = 0.3, 0.5, 1.0 and 1.5 L min^{-1}

Moreover, by examining the values of bulk Fr number, some hints may be obtained on the ranges of operating parameters for the SMT storage tank for stable and calm thermocline evolution. Note that the Fr number considers both the inertia force (Q_{in}) and the buoyancy force (ΔT). For small Fr numbers (e.g., Fr<3), the flow and temperature disturbances induced by the inflowing thermal jet are relatively small so that simple inlet & outlet ports could work well. Nevertheless, for higher Fr number conditions (e.g., Fr>3), additional structuration of the inlet & outlet port/manifold has to be considered to mitigate the thermocline decay due to strong inlet mixing. The higher the Fr number, the geometry adaptation of the flow diffusers is more needed, even indispensable, by using some optimization algorithms. In that way, the SMT storage tank could be operated under some harsh working conditions with a good performance.

Figure 14 shows the calculated exergy efficiency η_{Ex} (cf. Eq. 25) of the storage tank, evaluating the usefulness of the stored energy in the TES tank by considering both the energy quantity and quality. Similar rankings of three ROPD combinations and similar influences of Q_{in} or ΔT as those for η_{dis} could be observed thus will not be repeated here. A noticeable feature is that the design point (Q_{in} = 1 L min^{-1}) turns out to be optimal for the optimized ROPDs from the viewpoint of exergy efficiency. While for S1 and S2, the optimal working flow rate is still Q_{in} = 0.5 L min^{-1}. In addition, better performance could be achieved by S5 at a higher T_h (343.15 K) than under its design point (333.15 K), highlighting again the benefit of larger ΔT in practice.

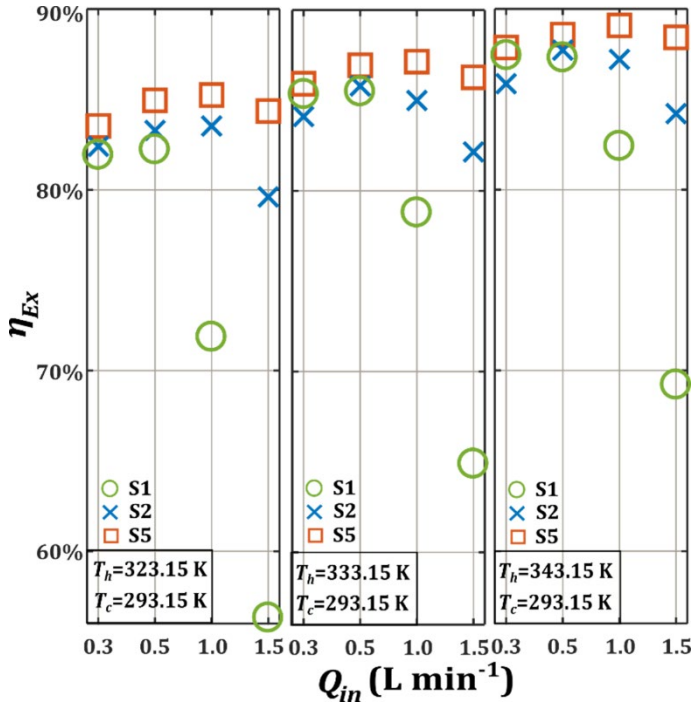

Figure 14. Exergy efficiency η_{Ex} of the SMT storage tank for different combinations of ROPDs. Conditions: T_h=323.15, 333.15, and 343.15 K, T_c=293.15 K, Q_{in} = 0.3, 0.5, 1.0 and 1.5 L·min^{-1}, discharging.

5. Conclusion and prospects

Numerical and experimental investigations have been performed for a cylindrical SMT storage tank subjected to charging or discharging operations. ROPDs with or without optimized configurations have been installed in the tank and their ability to mitigate the disturbances induced by the entering thermal jet has been tested. Main conclusions are summarized as follows:

- The optimization algorithm proposed in [34] and conceived ROPDs have been experimentally validated and proved to be effective, efficient, robust and simple to implement.
- A larger ΔT favors the thermal stratification for the charging process. For the discharging, the influence is less obvious under the tested conditions. The difference could be due to the heat loss despite the insulation of the tank.
- The charging or discharging efficiency of the storage tank with simple inlet/outlet ports falls sharply when Q_{in} is higher than 1 L·min^{-1} (Re_{tank}>167). The performance deterioration could be limited to a certain extent when ROPDs are used.
- The combined effect of Q_{in} (inertial force) and ΔT (buoyancy force) could be characterized by the bulk Fr number. A stable range of the operating parameters for the SMT storage tank (with simple inlet/out ports) has been determined. For small Fr numbers (e.g., Fr<3), the flow and temperature disturbances induced by the inflowing thermal jet are relatively small. For higher Fr number conditions (e.g., Fr>3), additional structuration of the inlet & outlet port/manifold

and geometry adaptation are essential to maintain the good performance of the SMT storage tank operated under some harsh working conditions.

- The combination of the optimized ROPDs could effectively mitigate the strong inertial force of thermal jet thereby significantly improve the global performances of thermocline tank. Compared to the simple inlet/outlet ports, the η_{Ex} could be improved from 56.3% to 84.2% (conditions: T_h=323.15 K, T_c=293.15 K, Q_{in} = 1.5 L·min^{-1}).

As prospects, a deeper understanding on the fluid mechanisms of the thermal jet (entrainment phenomenon [46]) and its influences on the heat transfer is very much needed. Therefore, simulations and the experimental measurements of local velocity and/or temperature fields using intrusive or non-intrusive optical-based methods [47] are our on-going work. The extension of the optimization algorithm to better fit other shapes of the storage tank remain to be addressed. Moreover, the effectiveness of diffusers under (partial) cyclic operations [48] is certainly an interesting aspect to be tested. The effect of inlet fluctuation on the performance of the storage tank issuing from its integration to the real environment can be studied by using some dynamic modeling techniques [49].

Acknowledgement

This work is supported by the French ANR within the project OPTICLINE (ANR-17-CE06–0013) and by the Chinese Scholarship Council (CSC) with the scholarship for Ms. Baoshan XIE (No. 201908430177).

Reference

[1] Commission E. National energy and climate plans EU countries' 10-year national energy and climate plans for 2021-2030 n.d. https://ec.europa.eu/info/energy-climate-change-environment/implementation-eu-countries/energy-and-climate-governance-and-reporting/national-energy-and-climate-plans_en#the-process.

[2] Seferlis P, Varbanov PS, Papadopoulos AI, Chin HH, Klemeš JJ. Sustainable design, integration, and operation for energy high-performance process systems. Energy 2021;224:120158. https://doi.org/10.1016/j.energy.2021.120158.

[3] Alva G, Lin Y, Fang G. An overview of thermal energy storage systems. Energy 2018;144:341–78. https://doi.org/10.1016/j.energy.2017.12.037.

[4] Pelay U, Luo L, Fan Y, Stitou D, Rood M. Thermal energy storage systems for concentrated solar power plants. Renew Sustain Energy Rev 2017;79:82–100. https://doi.org/10.1016/j.rser.2017.03.139.

[5] Pelay U, Luo L, Fan Y, Stitou D, Castelain C. Integration of a thermochemical energy storage system in a Rankine cycle driven by concentrating solar power: Energy and exergy analyses. Energy 2019;167:498–510. https://doi.org/10.1016/j.energy.2018.10.163.

[6] IRENA. Innovation Outlook: Thermal Energy Storae. Abu Dhabi: 2020.

[7] Ma Z, Li M-J, Zhang KM, Yuan F. Novel designs of hybrid thermal energy storage system and operation strategies for concentrated solar power plant. Energy 2021;216:119281. https://doi.org/10.1016/j.energy.2020.119281.

[8] Cascetta M, Petrollese M, Oyekale J, Cau G. Thermocline vs. two-tank direct thermal storage system for concentrating solar power plants: A comparative techno-economic assessment. Int J Energy Res 2021:er.7005. https://doi.org/10.1002/er.7005.

[9] Xie B, Baudin N, Soto J, Fan Y, Luo L. Wall impact on efficiency of packed-bed thermocline thermal energy storage system. Energy 2022;247:123503. https://doi.org/10.1016/j.energy.2022.123503.

[10] Ortega-Fernández I, Zavattoni SA, Rodríguez-Aseguinolaza J, D'Aguanno B, Barbato MC. Analysis of an integrated packed bed thermal energy storage system for heat recovery in compressed air energy storage technology. Appl Energy 2017;205:280–93. https://doi.org/10.1016/j.apenergy.2017.07.039.

[11] Gajbhiye P, Salunkhe N, Kedare S, Bose M. Experimental investigation of single media thermocline storage with eccentrically mounted vertical porous flow distributor. Sol Energy 2018;162:28–35. https://doi.org/10.1016/j.solener.2017.12.062.

[12] Dahash A, Ochs F, Janetti MB, Streicher W. Advances in seasonal thermal energy storage for solar district heating applications: A critical review on large-scale hot-water tank and pit thermal energy storage systems. Appl Energy 2019;239:296–315. https://doi.org/10.1016/j.apenergy.2019.01.189.

[13] Vannerem S, Neveu P, Falcoz Q. Experimental investigation of the impact of fluid distribution on thermocline storage performance. J Energy Storage 2022;52:104864. https://doi.org/10.1016/j.est.2022.104864.

[14] Dehghan AA, Barzegar A. Thermal performance behavior of a domestic hot water solar storage tank during consumption operation. Energy Convers Manag 2011;52:468–76. https://doi.org/10.1016/j.enconman.2010.06.075.

[15] Advaith S, Parida DR, Aswathi KT, Dani N, Chetia UK, Chattopadhyay K, et al. Experimental investigation on single-medium stratified thermal energy storage system. Renew Energy 2021;164:146–55. https://doi.org/10.1016/j.renene.2020.09.092.

[16] Li S, Zhang Y, Li Y, Zhang X. Experimental study of inlet structure on the discharging performance of a solar water storage tank. Energy Build 2014;70:490–6. https://doi.org/10.1016/j.enbuild.2013.11.086.

[17] Tang J, OuYang Z, Shi Y. Diffuser design and experimental research of a large-scale chilled water storage system. Energy Sources, Part A Recover Util Environ Eff 2021;43:1456–67. https://doi.org/10.1080/15567036.2020.1804013.

[18] Bouzaher MT, Bouchahm N, Guerira B, Bensaci C-E, Lebbi M. On the thermal stratification inside a spherical water storage tank during dynamic mode. Appl Therm Eng 2019;159:113821. https://doi.org/10.1016/j.applthermaleng.2019.113821.

[19] Afrin S, Kumar V, Bharathan D, Glatzmaier GC, Ma Z. Computational analysis of a pipe flow distributor for a thermocline based thermal energy storage system. J Sol Energy Eng Trans ASME 2014;136. https://doi.org/10.1115/1.4024927.

[20] Parida DR, Advaith S, Dani N, Basu S. Assessing the impact of a novel hemispherical diffuser on a single-tank sensible thermal energy storage system. Renew Energy 2022;183:202–18. https://doi.org/10.1016/j.renene.2021.10.099.

[21] Shah LJ, Andersen E, Furbo S. Theoretical and experimental investigations of inlet stratifiers for solar storage tanks. Appl Therm Eng 2005;25:2086–99. https://doi.org/10.1016/j.applthermaleng.2005.01.011.

[22] Dragsted J, Furbo S, Dannemand M, Bava F. Thermal stratification built up in hot water tank with different inlet stratifiers. Sol Energy 2017;147:414–25. https://doi.org/10.1016/j.solener.2017.03.008.

[23] Gajbhiye P, Kedare S, Bose M. Experimental analysis of parameters influencing thermal stratification in single media single tank storage system with flow distributor. Therm Sci Eng Prog 2022;30:101243. https://doi.org/10.1016/j.tsep.2022.101243.

[24] Chung JD, Cho SH, Tae CS, Yoo H. The effect of diffuser configuration on thermal stratification in a rectangular storage tank. Renew Energy 2008;33:2236–45. https://doi.org/10.1016/j.renene.2007.12.013.

[25] Karim MA. Experimental investigation of a stratified chilled-water thermal storage system. Appl Therm Eng 2011;31:1853–60. https://doi.org/10.1016/j.applthermaleng.2010.12.019.

[26] García-Marí E, Gasque M, Gutiérrez-Colomer RP, Ibáñez F, González-Altozano P. A new inlet device that enhances thermal stratification during charging in a hot water storage tank. Appl Therm Eng 2013;61:663–9. https://doi.org/10.1016/j.applthermaleng.2013.08.023.

[27] Wang S, Davidson JH. Performance of a rigid porous-tube stratification manifold in comparison to an inlet pipe. Sol Energy 2017;146:298–308. https://doi.org/10.1016/j.solener.2017.02.045.

[28] Hosseinnia SM, Akbari H, Sorin M. Numerical analysis of thermocline evolution during charging phase in a stratified thermal energy storage tank. J Energy Storage 2021;40:102682. https://doi.org/10.1016/j.est.2021.102682.

[29] Bahnfleth WP, Song J. Constant flow rate charging characteristics of a full-scale stratified chilled water storage tank with double-ring slotted pipe diffusers. Appl Therm Eng 2005;25:3067–82. https://doi.org/10.1016/j.applthermaleng.2005.03.013.

[30] Chandra YP, Matuska T. Numerical prediction of the stratification performance in domestic hot water storage tanks. Renew Energy 2020;154:1165–79. https://doi.org/10.1016/j.renene.2020.03.090.

[31] Li G. Sensible heat thermal storage energy and exergy performance evaluations. Renew Sustain Energy Rev 2016;53:897–923. https://doi.org/10.1016/j.rser.2015.09.006.

[32] Yaïci W, Ghorab M, Entchev E, Hayden S. Three-dimensional unsteady CFD simulations of a thermal storage tank performance for optimum design. Appl Therm Eng 2013;60:152–63. https://doi.org/10.1016/j.applthermaleng.2013.07.001.

[33] Wang Z, Zhang H, Dou B, Huang H, Wu W, Wang Z. Experimental and numerical research of thermal stratification with a novel inlet in a dynamic hot water storage tank. Renew Energy 2017;111:353–71. https://doi.org/10.1016/j.renene.2017.04.007.

[34] Lou W, Fan Y, Luo L. Single-tank thermal energy storage systems for concentrated solar power: Flow distribution optimization for thermocline evolution management. J Energy Storage 2020;32:101749. https://doi.org/10.1016/j.est.2020.101749.

[35] Nelson JEB, Balakrishnan AR, Srinivasa Murthy S. Experiments on stratified chilled-water tanks. Int J Refrig 1999;22:216–34. https://doi.org/10.1016/S0140-7007(98)00055-3.

[36] Shaikh W, Wadegaonkar A, Kedare SB, Bose M. Numerical simulation of single media thermocline based storage system. Sol Energy 2018;174:207–17. https://doi.org/10.1016/j.solener.2018.08.084.

[37] Engineering ToolBox. Water - Thermal Conductivity 2018. https://www.engineeringtoolbox.com/water-liquid-gas-thermal-conductivity-temperature-pressure-d_2012.html (accessed March 4, 2021).

[38] Engineering ToolBox. Water - Density, Specific Weight and Thermal Expansion Coefficient 2003. https://www.engineeringtoolbox.com/water-density-specific-weight-d_595.html (accessed March 4, 2021).

[39] Assari MR, Basirat Tabrizi H, Savadkohy M. Numerical and experimental study of inlet-outlet locations effect in horizontal storage tank of solar water heater. Sustain Energy Technol Assessments 2018;25:181–90. https://doi.org/10.1016/j.seta.2017.12.009.

[40] Haller MY, Cruickshank CA, Streicher W, Harrison SJ, Andersen E, Furbo S. Methods to determine stratification efficiency of thermal energy storage processes – Review and theoretical comparison. Sol Energy 2009;83:1847–60. https://doi.org/10.1016/j.solener.2009.06.019.

[41] Fasquelle T, Falcoz Q, Neveu P, Hoffmann J-F. A temperature threshold evaluation for thermocline energy storage in concentrated solar power plants. Appl Energy 2018;212:1153–64. https://doi.org/10.1016/j.apenergy.2017.12.105.

[42] Kim DH, Yoon SH, Kim Y, Song CH, Lee KH, Choi JS. Experimental studies of the discharge performance of single-medium TES for CSP applications. Appl Therm Eng 2017;127:499–507. https://doi.org/10.1016/j.applthermaleng.2017.08.057.

[43] Zanganeh G, Pedretti A, Haselbacher A, Steinfeld A. Design of packed bed thermal energy storage systems for high-temperature industrial process heat. Appl Energy 2015;137:812–22. https://doi.org/10.1016/j.apenergy.2014.07.110.

[44] Cheng X, Zhai X. Thermal performance analysis and optimization of a cascaded packed bed cool thermal energy storage unit using multiple phase change materials. Appl Energy 2018;215:566–76. https://doi.org/10.1016/j.apenergy.2018.02.053.

[45] Carmona M, Rincón A, Gulfo L. Energy and exergy model with parametric study of a hot water storage tank with PCM for domestic applications and experimental validation for multiple operational scenarios. Energy Convers Manag 2020;222. https://doi.org/10.1016/j.enconman.2020.113189.

[46] Kaloudis E, Grigoriadis DGE, Papanicolaou E. Numerical simulations of constant-influx gravity currents in confined spaces: Application to thermal storage tanks. Int J Therm Sci 2016;108:1–16. https://doi.org/10.1016/j.ijthermalsci.2016.04.018.

[47] Wei M, Boutin G, Fan Y, Luo L. Numerical and experimental investigation on the realization of target flow distribution among parallel mini-channels. Chem Eng Res Des 2016;113. https://doi.org/10.1016/j.cherd.2016.06.026.

[48] Elfeky KE, Mohammed AG, Wang Q. Cycle cut-off criterion effect on the performance of cascaded, sensible, combined sensible-latent heat storage tank for concentrating solar power plants. Energy 2021;230:120771. https://doi.org/10.1016/j.energy.2021.120771.

[49] PELAY U, LUO L, FAN Y, STITOU D. Dynamic modeling and simulation of a concentrating solar power plant integrated with a thermochemical energy storage system. J Energy Storage 2020;28:101164. https://doi.org/10.1016/j.est.2019.101164.